ACS APPLIED MATERIALS & INTERFACES

Research Article

www.acsami.org

Facile Synthesis of High-Crystallinity Graphitic Carbon/Fe_3C Nanocomposites As Counter Electrodes for High-Efficiency Dye-Sensitized Solar Cells

Yongping Liao, Kai Pan,* Lei Wang, Qingjiang Pan, Wei Zhou, Xiaohuan Miao, Baojiang Jiang, Chungui Tian, Guohui Tian, Guofeng Wang, and Honggang Fu*

Key Laboratory of Functional Inorganic Material Chemistry, Ministry of Education, School of Chemistry and Materials Science, Heilongjiang University, Harbin 150080, People's Republic of China

Supporting Information

ABSTRACT: Because of the advantages of both rapid electron transport of graphitic carbon and high catalytic performance of Fe_3C nanoparticle, highly crystalline graphitic carbon (GC)/Fe_3C nanocomposites have been prepared by a facile solid-state pyrolysis approach and used as counter electrode materials for high-efficiency dye-sensitized solar cells (DSSCs). The content of Fe_3C in the composites can be modified by different hydrochloric acid treatment time. In comparison with pure highly crystalline GC, the DSSC based on GC/Fe_3C nanocomposite with 13.5 wt % Fe_3C content shows higher conversion efficiency (6.04%), which indicates a comparable performance to the Pt-based DSSC (6.4%) as well. Moreover, not only does our DSSCs have comparable performance to that of the Pt-based DSSC (6.4%), but also is more cost-effective as well. To evaluate the chemical catalysis and stability of nanocomposite counter electrodes toward I_3^- reduction and the interfacial charge transfer properties, GC/Fe_3C nanocomposites have been quantitatively characterized by cyclic voltammetry, electrochemical impedance spectra, and Tafel polarization curve. All the results have revealed that the GC/Fe_3C nanocomposite counter electrodes can exhibit high catalytic performance and fast interfacial electron transfer, which can be acted as a very promising and high cost-effective materital for DSSCs.

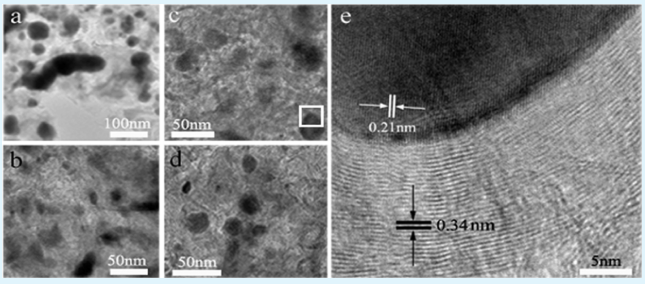

KEYWORDS: *graphitic carbon, Fe_3C, counter electrode, catalysis, interfacial charge transfer*

1. INTRODUCTION

Solar light is considered to be one of the ideal renewable energy sources and has already been widely used in the manufacture and human living because of its endless supply without district limit. Since the outstanding work of M. Grätzel was reported in 1991, much attention has been focused on the dye-sensitized solar cells (DSSCs) because of its low cost, nonpollution, easy fabrication and relatively high power conversion efficiency (η).[1−5] Generally, in DSSCs, there are several parts such as nanocrystalline semiconductor oxide photoanode, dye sensitizer, redox couple electrolyte, and counter electrode (i.e., cathode).[6,7] Among them, the counter electrode performs a function of transferring photogenerated electrons from the external circuit back to the redox shuttle and catalyzing the reduction of triiodide ion.[8] Platinum (Pt) nanopaticle is generally used as the cathode material due to its excellent catalytic activity in reduction of I_3^- and high light reflection ability. However, Pt is a quite rare metal with high price, and it is easily corroded in electrolyte, which restricted the wide range of commercial application of the DSSCs in the future.[9] Therefore, it is urgent to develop a kind of new cathode material with low cost, high catalytic activity, high electrical conductivity, and strong corrosion resistance to replace Pt.

Recently, a series of substitutes for Pt have been explored such as carbon materials, including carbon black,[10] activated carbon,[11] carbon nanotubes,[12,13] graphene,[14−17] and graphitic carbon (GC),[18] These carbon materials are used as the cathode materials to replace Pt because of their relatively low-cost, easy preparation and preferable electron-transport ability. Among them, due to the exceptional electrical and mechanical properties, high thermal and chemical stability, GC is a promising candidate for catalyst support research.[19] However, the carbon materials suffer from low intrinsic electrocatalytic activity in reducing triiodide, leading to a low efficiency of DSSCs. Therefore, much focus was given to transition metal compounds, such as transition metal carbide,[20,21] nitride,[22,23] oxide,[24−26] sulfide.[27−29] Compared with Pt, these transition metal compounds show excellent catalytic performances but in poor electron transport efficiency between nanoparticles and

Received: January 14, 2013
Accepted: April 8, 2013
Published: April 8, 2013

   dx.doi.org/10.1021/am4001584 | ACS Appl. Mater. Interfaces 2013, 5, 3663−3670

conductive substrate resulting in nanoparticle aggregation, which hinder their applications in DSSCs.[30] To solve these drawbacks of the individual carbon materials and transition metal compounds, many attempts have been focused on the inorganic metal compound nanoparticle/carbon material composite, for instance, TiN/conductive carbon black,[31] CoS/MWCNT,[32] TiN/carbon nanotubes,[33] MoC/WC/VC/ordered mesoporous nanocarbon,[23,34] nitrides/graphene,[35] phosphides/graphene,[36] sulfide/graphene,[37] etc. As a result, combining nanocarbon material with inorganic metal compound shows a better performance in both electrocatalytic activity and electron transport capacity. The reason is these nanocarbon materials in the composites provide fast electron-transport network and effective support for the highly active nanoparticles. Meanwhile, the inorganic metal compounds play a role in increasing electrocatalytic activity of cathode. That is, with the beneficial effect from inorganic metal nanocompound and carbon nanomaterials composite, a better performance is obtained in DSSCs.

Besides the above-mentioned inorganic metal compounds combined with carbon nanomaterials, the Fe_3C is a very promising catalytic material for cathode in DSSCs. Primarily, in Fe_3C lattice, carbon atoms occupy the interstices among close-packed iron atoms, and the presence of carbon atom makes iron carbide with excellent mechanical strength and catalytic activity in energy conversion processes.[38,39] Besides catalytic advantage, the magnetic property of iron carbide has been gained more attentions. However, it is much less investigated than WC, MoC, or VC, mainly because of the difficulty in its synthesis process. Therefore, it will be preferable to obtain GC/Fe_3C nanoparticle composite in an easy and in situ method. Accoring to previous reports, the content of inorganic metal compound is uncontrollable in the carbon material/inorganic metal compound. To adjust the content of Fe_3C in nanocomposite freely is a key point as well. Furthermore, the price of the iron is much lower than tungsten, molybdenum, or vanadium in the commercial view.

In the present work, we in situ synthesized a GC/Fe_3C nanoparticle composites via solid-state pyrolysis process, The Fe_3C content in composite was controlled by different hydrochloric acid treating time. The composite with various Fe_3C concentration was used as the cathode in DSSCs. The results show the composites will perform a higher power conversion efficiency than the pure GC by improving the electron-transport between the electrolyte and counter electrode, and enhancing the electrocatalytic activity in reducing triiodide.

2. EXPERIMENTAL SECTION

2.1. Chemicals. The commercial TiO_2 powder (P25, Degussa, Germany), N-methyl-2-pyrrolidone (NMP, 99%), polyvinylidene fluoride (PVDF), and polyacrylic weak-acid cation-exchanged resin (AC resin) were purchased from standard source. The transparent conducting glass (TCO, fluorine doped SnO_2 layer, 20 Ω/square, Nippon sheet glass, Japan) was used as electrode substrate. The used Ru complex dye was cis-bis(isothiocyanato) bis (2,2′-bipyridyl-4,4′-dicarboxylato) ruthenium(II) bis- tetrabutylammonium (N719, Solaronix SA, Switzerland). The redox shuttle electrolyte was composed of 0.1 M LiI (anhydrous, 99%, Acros), 0.05 M I_2 (anhydrous, 99.8%), 0.5 M tertbutylpyridine (99%, Aldrich), and 0.6 M 1-propyl-2, 3-dimethylimidazolium iodide (99%) in acetonitrile (99%, Fluka). All the chemicals were at least reagent grade and used as received without further purification. Milli-Q water with a resistivity of 18 MΩ/cm was used in all the experiments.

2.2. Synthesis of GC/Fe_3C Composite. The highly crystalline GC/Fe_3C composites with controllable Fe_3C nanoparticle content are in situ prepared via solid-state pyrolysis process, which is similar to our previous work by only changing the exchange quantity of Fe^{2+}, the carbonized temperature and post-treatment time with hydrochloric acid.[40] First, AC resin was added to 0.15 M aqueous $FeCl_2$ solution, and the solution was stirred for 10 h under the N_2 atmosphere. After centrifuging/washing cycles several times the solid sample was separated and dried in vacuum to introduce more Fe^{2+} into the AC resin. The obtained composite was carbonized in N_2 at 900 °C atmosphere for 30 min, then the GC/Fe_3C/Fe composite was obtained. For the controllable content of the Fe_3C nanoparticles and complete removal of iron metal, the GC/Fe_3C/Fe composite was treated by 5 wt % HCl for different time (10 min, 12 and 15 min), followed by Fe_3C content of 21.9, 13.5, and 9.4%, respectively,. As a reference, the pure highly crystalline GC was prepared according to our previous work as well.[40]

2.3. Fabrication of GC/Fe_3C Composite Cathode and Assembly of DSSCs. To improve the dispersion of samples, we treated the as-prepared GC/Fe_3C composite by ball-milling process at 140 rpm for 8 h first, followed by. adding 1 mL NMP solvent contained 5 wt % PVDF to the treated composite. The resulting mixture was stirred for 4 h to obtain GC/Fe_3C composite paste. The cathode was fabricated via the doctor-blade method, and then dried at 160 °C under the protection of N_2 atmosphere for 2 h. Another three cathodes with different Fe_3C nanoparticle contents of 21.9, 13.5, and 9.4%, and the pure GC were prepared in same routine. A mirrorlike Pt cathode was fabricated by pyrolysis of H_2PtCl_6 isopropanol solution at 385 °C for 30 min.[41] The obtained counter electrodes with different Fe_3C nanoparticle content of 21.9, 13.5, and 9.4%, the pure GC counter electrode and the Pt counter electrode were labeled as E_1, E_2, E_3, E_{GC}, and E_{Pt}, respectively. The thickness of the as-prepared film cathodes was 7 μm as characterized by scanning electron microscope (SEM).

The dye-sensitized TiO_2 photoanodes were prepared according to previous work.[42] The DSSCs were assembled by injecting redox shuttle electrolyte into the space between the photoanodes and cathodes. The two electrodes were adhered together with epoxy resin to prevent leakage of the electrolyte solution. The fabricated DSSCs based on cathodes of E_1, E_2, E_3, E_{GC}, and E_{Pt} were labeled as C_1, C_2, C_3, C_{GC}, and C_{Pt}, respectively. To gain insight into the effect of sheet resistance and catalytic properties of the counter electrode and remove the impact of the photoanode, we fabricated the dummy cells consisted of two identical counter electrodes. And the dummy cells with two identical E_1, E_2, E_3, and E_{Pt} were labeled as DC_1, DC_2, DC_3, and DC_{Pt}. The active area of both DSSCs and dummy cells are 0.12 cm^2.

2.4. Characterization. The composition of the composite nanomaterials was characterized by X-ray diffraction (XRD) using a Rigaku D/max-IIIB diffractometer with Cu Kα (λ = 1.5406 Å). Thermogravimetric Analysis (TGA) measurements were carried out to examine the phase changes using a Rheometric Scientific DSC QC (TA, USA). About 20 mg of the dried complexes were heated from room temperature to 1000 °C with a constant heating rate of 10 °C min^{-1} under air atmosphere. Raman spectra were recorded with a HR 800 micro-Raman spectrometer (Jobin−Yvon, France) excited by an argon ion laser with a wavelength of 457.9 nm. Transmission electron microscopy (TEM) experiment was performed on a JEM-3010 electron microscope (JEOL, Japan) with an acceleration voltage of 200 kV. Carbon-coated copper grids were used as the sample holders. The Nitrogen adsorption/desorption isotherms were measured by TriStar II 3020 at 77 K.

Photovoltaic measurements were carried out with a solar simulator (Oriel, USA) equipped with an AM 1.5G filter (Oriel, USA). The power of the simulated light was calibrated to 100 mW cm^{-2} by using a solar simulator radiometer (Oriel, USA). Photocurrent−photovoltage (J−V) curves were recorded by applying an external photomask of 0.12 cm^2 and measuring the generated photocurrent with a BAS100B electrochemical analyzer (Bioanalytical Systems Inc., USA). The electrochemical impendence spectroscopy (EIS) experi-

ments were conducted in dummy cells by using a computer-controlled potentiostat (Zahner Elektrik, Germany) and carried out by applying sinusoidal perturbations of 10 mV under bias of −0.8 V with the frequency range from 100 mHz to 1 MHz. The obtained spectra were fitted with ZsimpWin software in terms of appropriate equivalent circuits. The Tafel polarization measurements were carried out with BAS100B electrochemical analyzer in a dummy cell with a scan rate of 50 mV s^{-1}. The cyclic voltammetry (CV) curves were carried out in a three−electrode system in a nitrogen−purged acetonitrile solution, which contains 0.1 M $LiClO_4$, 10 mM LiI and 1 mM I_2 with a scan rates from 4 to 100 mV s^{-1} in BAS100B electrochemical analyzer. Thereinto, Pt is worked as an auxiliary electrode, versus the Ag/Ag^+ reference electrode.

3. RESULTS AND DISCUSSION

3.1. Structural Characterization of Highly Crystalline GC/Fe_3C Nanocomposite. The crystallinity of cathode nanomaterials has an important effect on the DSSCs performance. XRD measurements were first carried out to characterize the crystallinity and structure of the GC/Fe_3C nanocomposite and pure GC (Figure 1). The diffraction peaks of the pure GC

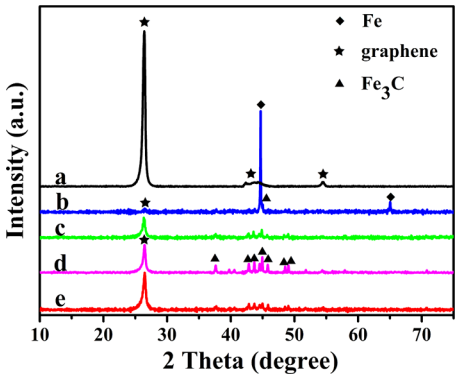

Figure 1. (a) XRD patterns of GC, (b) GC/Fe_3C/Fe composite without HCl treatment, and GC/Fe_3C composite with Fe_3C nanoparticle weight ratio of (c) 21.9, (d) 13.5, and (e) 9.4%.

around 2θ=26.2°, 42.5°, and 54.6° is strong, corresponding to (002), (100), and (004) planes of graphite (JCPDS No. 41−1487). It indicates that the GC had a high crystallinity (Figure 1a). But for the prepared samples that were not treated with HCl, besides the weak diffraction peak of GC at 2θ = 26.2°, and that of Fe_3C at 2θ = 45.0°, there exists a strong diffraction peak at 2θ = 44.7°, that corresponded to (110) plane of Fe (JCPDS No. 87−0722) (Figure 1b). This indicates that much iron exists in the prepared sample before HCl treatment. After HCl treatment for different time of 10, 12, and 15 min, diffraction peaks of Fe disappear, implying the iron had been completed removed. And besides the peak of GC at 26.2°, there only remain the diffraction peaks at around 2θ = 37.8, 39.9, 40.7, 42.9, 43.7, 44.6, 45.1, 46.0, 48.7, and 49.1°, which correspond to (210), (002), (201), (211), (102), (220), (031), (112), (131), and (221) planes of Fe_3C nanoparticles (JCPDS No. 89−2867), respectively (Figure 1c−e).

To quantificationally analyze the content of Fe_3C nanoparticles in the GC/Fe_3C nanocomposite, we have performed TGA for these samples with different HCl treatment time. The TG curves of the corresponding composite in an air stream at a heating rate of 10 °C min^{-1} to the final temperature of 1000 °C are shown Figure 2. It can be seen that the sample weight decreases below 205 °C due to a dehydration reaction, the weight decreases between 200 and 400 °C should be ascribed

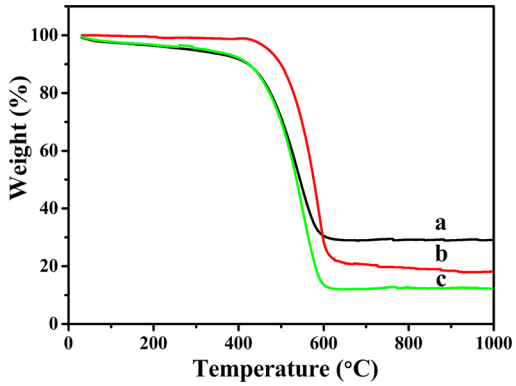

Figure 2. TGA curves of the GC/Fe_3C nanocomposite with HCl treating different time: (a) 10, (b) 12, and (c) 15 min.

to the decomposion of functional groups adsorbed on the surface of GC, and the weight decreases between 400 and 800 °C should be ascribed to the oxidation of GC and Fe_3C. The GC becomes CO_2 gas and Fe_3C nanoparticles are oxidated into Fe_2O_3. They samples are pure. The difference is only due to the adsorption amount of H_2O and the functional groups. The GC/Fe_3C composites with different Fe_3C contents are prepared with different HCl treatment time, so the surface state of these composites are different. The different surface states will result in different adsorption amount for H_2O and functional groups. The Fe_3C nanoparticle loading (x %) can be calculated by the following eq 1.

$$x\% = \frac{2}{3}\frac{m_2}{m_1}\frac{M_{Fe_3C}}{M_{Fe_2O_3}} \times 100\% \quad (1)$$

Where m_1 and m_2 are the mass of GC/Fe_3C nanocomposite and residual Fe_2O_3 nanoparticles, respectively. $M$$Fe_3C$ and $M$$Fe_2O_3$ is the molecular mass of Fe_3C and Fe_2O_3, respectively. The mass percentage of residual Fe_2O_3 is (a) 29.2%, (b) 18.0%, and (c) 12.5%, so the Fe_3C content is 21.9, 13.5, and 9.4 wt % for the GC/Fe_3C composite with HCl treatment time of 10, 12, and 15 min, respectively.

Because the GC/Fe_3C composite with the Fe_3C content of 13.5% have the different surface state with the other GC/Fe_3C composite, it possesses the different TGA behaviors with the others. Maybe the sample a and c have similar surface state, they possess the similar TGA behaviors.

Raman spectroscopy, very sensitive response to the crystallinity and microstructure of materials, is usually used to unambiguously distinguish the local order characteristics of nanomaterials. The peak positions are interrelated not only to crystallinity but also to the morphology of materials. Figure 3 shows the Raman spectra of pure GC (a), GC/Fe_3C nanocomposite with different Fe_3C content of 9.4% (b), 13.5% (c), and 21.9% (d), respectively. The three Raman characteristic response peaks at 1357, 1573, and 2719 cm^{-1} correspond to the D-band, G-band, and 2D-band of GC (Figure 3a). Meanwhile, the peaks at low wave numbers of 216, and 277 cm^{-1} are ascribed to Fe_3C nanoparticle (Figure 3b−d). All the I_G/I_D values are larger than 2.0, implying a quite high crystalline structure of the obtained GC, which is consistent with the XRD results.[43]

TEM images have also been used to further analyze the features of the obtained GC/Fe_3C nanocomposite. Figure 4 shows the TEM images of GC/Fe_3C/Fe composite without HCl treatment (a), GC/Fe_3C nanocomposite with Fe_3C

dx.doi.org/10.1021/am4001584 | ACS Appl. Mater. Interfaces 2013, 5, 3663−3670

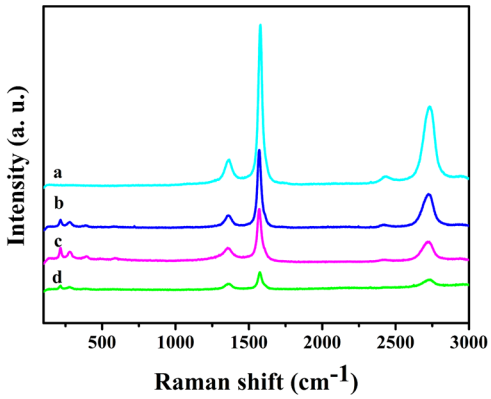

Figure 3. (a) Raman spectra of pure GC, GC/Fe_3C nanocomposite with Fe_3C content of (b) 21.9, (c) 13.5, and (d) 9.4%, respectively.

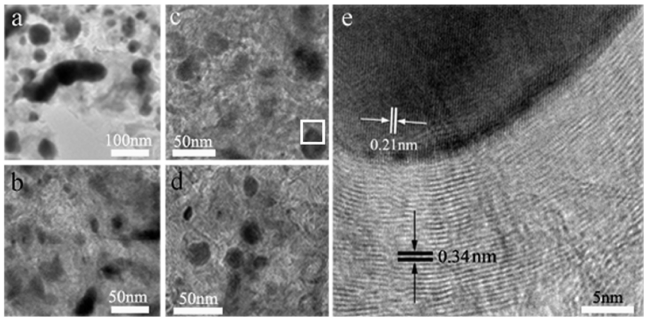

Figure 4. Typical TEM images of GC/Fe_3C/Fe composite without HCl treatment (a), GC/Fe_3C nanocomposite with Fe_3C content of (b) 21.9, (c) 13.5, and (d) 9.4%. (e) HRTEM image of GC/Fe_3C composite with the content of 13.5%.

content of 21.9% (b), 13.5% (c), and 9.4% (d), respectively. It can be seen that the GC possesses the curved nanostructure, and there are many Fe_3C and Fe nanoparticles supported on the GC (Figure 4a). For the purpose of investgating the effect of Fe_3C content on the performance of DSSCs, the GC/Fe_3C/Fe composite was treated with HCl for different time. The amount of Fe_3C decreases with increased treatment time, along with the complete disappearance of Fe nanoparticles (Figure 4b–d). This agreed with the XRD and TGA results. The Fe_3C nanoparticles are loaded on the GC, and the size of the Fe_3C nanoparticles is about 30 nm. HRTEM image of GC/Fe_3C nanocomposite with the Fe_3C content of 13.5% is shown in Figure 4e. It could be seen that well-crystallized structures with lattice fringes of about 0.34 and 0.21 nm, corresponding to an interplanar spacing of graphite (002) and Fe_3C (211) crystal plane, respectively. From the above data, it can be concluded, to a certain extent, the GC/Fe_3C nanocomposite with controllable Fe_3C nanoparticle content is formed. And the Fe_3C nanoparticles are well-loaded on the GC. This nanocomposite would have a better electrocatalytic activity because it combines the advantages of the rapid electron transport of GC and the better catalytic activity of Fe_3C nanoparticles.

Figure 5 depicts the N_2 sorption of isotherm of GC/Fe_3C with controllable Fe_3C content and the GC/Fe_3C/Fe sample. The surface areas of these samples calculated by the BET method are shown in Table 1. The surface area of the GC/Fe_3C/Fe composite is 58.98 m^2 g^{-1}, which is small due to the existence of much iron. After the iron is removed, the surface areas become large. The GC/Fe_3C composite with the Fe_3C

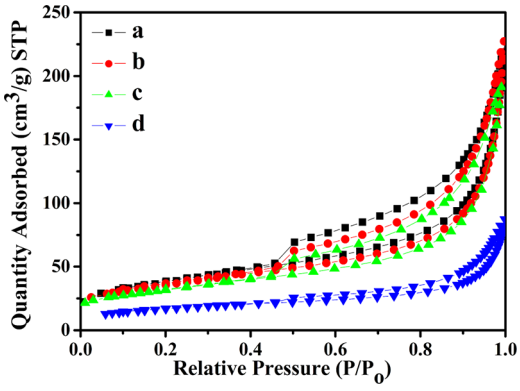

Figure 5. Nitrogen adsorption–desorption isotherms of composite with Fe_3C content of (a) 21.9, (b) 13.5, and (c) 9.4%, and (d) GC/Fe_3C/Fe without HCl treatment.

Table 1. BET Surface Areas of Different GC-Based Nanocomposite

samples	S_{BET}[a] (m^2 g^{-1})
GC/Fe_3C/Fe without HCl treat	58.98
GC/Fe_3C with Fe_3C content of 21.9%	132.44
GC/Fe_3C with Fe_3C content of 13.5%	124.55
GC/Fe_3C with Fe_3C content of 9.4%	111.84

[a]BET (Brunauer–Emmett–Teller) surface area.

content of 21.9, 13.5, and 9.4% possess the surface areas of 132.44, 124.55, and 111.84 m^2 g^{-1}, respectively. With the increase in HCl treating time, the surface areas of GC/Fe_3C nanocomposite decrease. But they still possess large surface areas that ensure more active sites for I^-/I_3^- redox reaction.

3.2. Photoelectrical Character of DSSCs. The as-prepared GC/Fe_3C nanocomposite and pure GC were used as the counter electrode to obtain high-efficiency DSSCs. The photocurrent density-photovoltage (J–V) curves of DSSCs are shown in Figure 6. The J–V curve of a reference DSSC with Pt

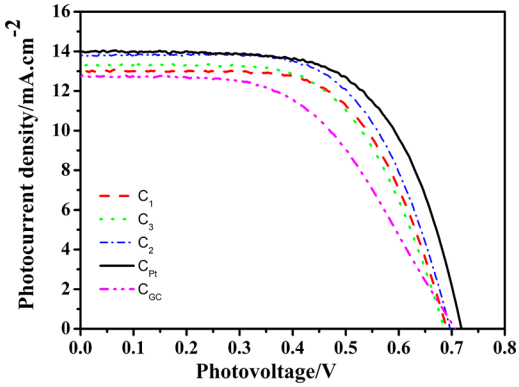

Figure 6. Typical photocurrent–-photovoltage curves of DSSCs based on GC/Fe_3C with different Fe_3C content (C_1, C_2, and C_3), GC (C_{GC}), and Pt (C_{pt}) counter electrode.

counter electrode is also presented.[44,45] These photovoltaic parameters, including open-circuit voltage (V_{oc}), short-circuit current density (J_{sc}), fill factor (FF), and photoelectrical conversion efficiency (η), are listed in Table 2. And each value is taken as an average of at least three samples. The DSSC (C_{GC}) with the pure GC counter electrode gets a η of 4.75%, whereas the DSSCs with GC/Fe_3C counter electrodes exhibit a

dx.doi.org/10.1021/am4001584 | ACS Appl. Mater. Interfaces 2013, 5, 3663–3670

Table 2. Detailed Photovoltaic Parameters for DSSCs Fabricated with Different Cathodes[a]

cells	V_{oc} (V)	J_{sc} (mA cm^{-2})	FF	η (%)
C_1	0.69 ± 0.02	13.00 ± 0.03	0.63 ± 0.08	5.65 ± 0.05
C_2	0.70 ± 0.01	13.77 ± 0.03	0.63 ± 0.02	6.04 ± 0.02
C_3	0.69 ± 0.05	13.33 ± 0.06	0.61 ± 0.05	5.56 ± 0.04
C_{GC}	0.71 ± 0.00	12.71 ± 0.04	0.53 ± 0.00	4.75 ± 0.00
C_{Pt}	0.72 ± 0.03	13.98 ± 0.01	0.64 ± 0.00	6.40 ± 0.01

[a] J_{sc}, short-circuit photocurrent; V_{oc}, open-circuit photovoltage; FF, fill factor; η, power conversion efficiency.

higher η. The C_1, C_2, and C_3 give η of 5.56, 6.04, and 5.65%, respectively. The V_{oc} value of the five DSSCs are almost the same, while the C_1, C_2, and C_3 exhibit the higher FF and J_{sc} values than that of the C_{GC}, which implying the positive effect of the addition of Fe_3C nanoparticles. Two reasons account for the higher FF and J_{sc} values. One is the lower diffusion impedance of the redox species for the GC/Fe_3C film than that for pure GC film, which contribute to the higher FF values. Another reason is related to the light absorption and scattering by the GC/Fe_3C film, which improves the reflection of the unabsorbed incident light from the counter electrode back to the TiO_2 photoanode. That is, the GC/Fe_3C counter electrode can reflect more nonabsorbtion incident lights, and then they are reabsorbed by the dye.[46] As a result, the DSSCs with GC/Fe_3C counter electrodes get higher J_{sc} than those with pure GC counter electrodes. What's more, the C_2 exhibits a η of 6.04%, which is higher than those of C_1 and C_3, and is comparable to that of the DSSCs with Pt counter electrodes (6.40%). This may result from the optimal interaction between the Fe_3C and GC, which is good for the electron transport between the electrolyte and counter electrode. In summary, the moderate Fe_3C nanoparticle content can effectively improve the performance of DSSCs. Figure 7 shows the consecutive CV curves of

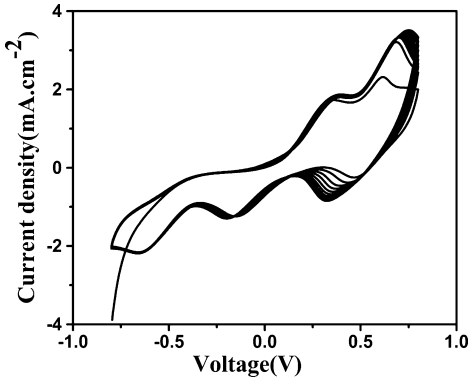

Figure 7. Consecutive 20 cyclic voltammograms for the GC/Fe_3C nanocomposite cathode with Fe_3C content of 13.5% at a scan rate of 25 mV s^{-1}.

the GC/Fe_3C nanocomposite electrode with Fe_3C content of 13.5%. It can be seen that no obvious current density decline and peak shifts are observed after a 20-cycle test, indicating that the GC/Fe_3C nanocomposite electrode possesses excellent electrochemical stability in the I^-/I_3^- electrolyte solution.

3.3. Key Factors Determining the Photoelectrical Properties. It is well-known that the performance of DSSCs is strongly dependent on the electrocatalytic activity and photoelectron transfer of counter electrode in the condition that other cell components remain identical.[47] That is, better catalytic activity and faster photoelectron transfer will lead to a higher η for DSSCs. In the following, the CV, EIS, and Tafel methods are used to further study the catalytic activity and electron transfer of cathode.

To further understand the reaction catalytic activity of the counter electrodes with different Fe_3C nanoparticle content, we have carried out CV of various counter electrodes. As well-known, the scan rate of CV measurement is an important factor to determine the cathodic current density. The faster scan rate will result in bigger cathodic current density. The CV curves of the GC/Fe_3C nanocomposite electrode with different Fe_3C content at the scan rate of 50 mV s^{-1} are shown in Figure 8.

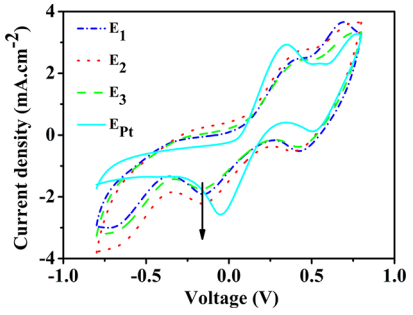

Figure 8. Cyclic voltammograms for the series of cathodes at a scan rate of 50 mV s^{-1} in 10 mM LiI, 1 mM I_2 acetonitrile solution containing 0.1 M $LiClO_4$ as the supporting electrolyte.

Two typical pairs of redox peaks are observed in all cases. The left pair in the low potential range is assigned as eq 2 and the right pair in the high potential range as eq 3

$$I_3^- + 2e^- \leftrightarrow 3I^- \quad (2)$$

$$3I_2 + 2e^- \leftrightarrow 2I_3^- \quad (3)$$

The electrochemical reduction of triiodide in the low potential range is the regeneration of the redox species on the counter electrode of DSSCs. Two pairs of redox peaks are observed for GC/Fe_3C cathodes, which are similar to that of Pt cathodes (Figure 8). This implies that the GC/Fe_3C cathode has the similar catalytic mechanism to Pt cathode. At the slow scan rate of 10 mV s^{-1}, the CVs of the GC/Fe_3C cathodes (see Figure S1 in the Supporting Information) differ not quite far from each other, which is similar to that at the scan rate of 25 mV s^{-1} (see Figure S2 in the Supporting Information). But when the scan rate reached to 50 mV s^{-1}, the cathodic current density of the GC/Fe_3C cathodes with 13.5% Fe_3C content (E_2) is the highest among the three Pt-free cathodes, suggesting that the E_2 has better electrocatalytic activity than the other This agrees with the $J-V$ results.

The CV curves of the GC/Fe_3C electrode with Fe_3C content of 13.5% are shown in Figure 9, which are obtained under different scan rates, ranging from 4 to 100 mV s^{-1}. The inset illustrates the current density of I^-/I_3^- reduction peaks as a function of scan rate. The linear relationship between the redox peak current density and the square root of scan rates suggests that the redox reaction on the GC/Fe_3C cathode is controlled by ionic diffusion in the electrolyte. It may be related to the transport of iodide species out of the counter electrode surface.[48]

EIS is a powerful tool to explore the electrochemical process and the interfacial charge transfer for the regeneration of a redox couple. In this work, EIS experiments were carried out

dx.doi.org/10.1021/am4001584 | ACS Appl. Mater. Interfaces 2013, 5, 3663−3670

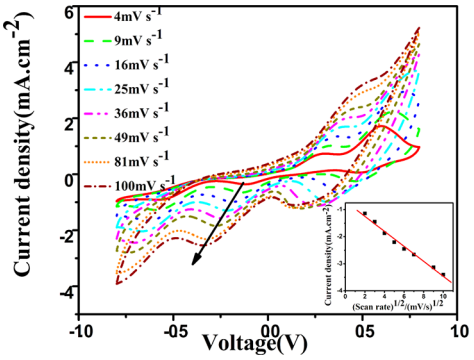

Figure 9. Cyclic voltammograms of the GC/Fe_3C nanocomposite with Fe_3C content of 13.5% under various scan rates. The inset shows the reduction peak current of the cathode as a function of scan rate.

with dummy cells fabricated with two identical counter electrodes under the bias voltage of −0.8 V.[37,49,50] The Nyquist plots of the dummy cells (DC_1, DC_2, DC_3, and DC_{pt}) are shown in Figure 10. The equivalent model fitting the

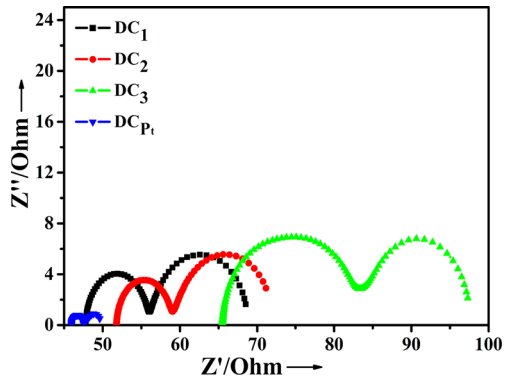

Figure 10. Nyquist plots of the dummy cells (DC_1, DC_2, DC_3, and DC_{pt}) fabricated with two identical E_1, E_2, E_3, and E_{Pt}. R_s, series resistance; R_{ct}, charge transfer resistance at the cathode/electrolyte interface; C_μ, capacitance at the cathode/electrolyte interface; Z_N, diffusion impedance of the redox couple (I_3^-/I^-).

Chart 1. Equivalent Circuit Used to Represent Interfaces in Composite Solar Cells Composed of TCO|GC-Fe_3C|I^-/I_3^-|GC-Fe_3C|TCO[a]

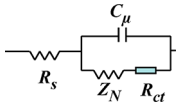

[a]The symbols R and C represent a resistance and a capacitance, respectively, Z_N represents the Warburg impedance relative to the Nernst diffusion of I_3^- in the electrolyte.

impedance spectra of the dummy cells is shown in Chart 1. The symbols of R and C represent a resistance and a capacitance, respectively. The high-frequency intercept on the real axis represents the series resistance (R_s). The left semicircle in the middle frequency can be attributed to the charge transfer resistance (R_{ct}) and the corresponding capacitance (C_μ) at the cathode/electrolyte interface.[51,52] The right semicircle in the low frequency can be assigned to the diffusion impedance (Z_N) of the redox couple (I^-/I_3^-) in the electrolyte, which can be expressed by eq 4

$$Z_N = \frac{W}{\sqrt{i\omega}}\tanh\left(\sqrt{\frac{i\omega}{K_N}}\right) \quad (4)$$

Where W is Warburg parameter, and $W = kT/n^2e^2CA\sqrt{D}$; $K_N = D/\delta^2$. D is the diffusion constant of I_3^-, C is the concentration of I_3^-, A is the counter electrode area, n is the number of electrons transferred in the reaction, k is the Boltzmann constant, e is the elementary charge, and δ is the thickness of the diffusion layer.[53]

The EIS data obtained by fitting the impedance spectra of DC_1, DC_2, DC_3, and DC_{pt} using the equivalent model of Chart 1 are summarized in Table 3. Each value for cell EIS

Table 3. Detailed EIS Parameters for Dummy Cells Fabricated with Two Identical Electrodes[a]

cells	R_s (Ω)	R_{ct} (Ω)	C_μ (μF)	Z_N (Ω)
DC_{Pt}	45.96	0.21	16.74	1.57
DC_1	47.80	6.45	4.33	7.88
DC_2	51.79	5.21	3.73	6.84
DC_3	65.49	7.74	1.12	8.30

[a]R_s, series resistance; R_{ct}, charge transfer resistance at the cathode/electrolyte interface; C_μ, capacitance at the cathode/electrolyte interface; Z_N, diffusion impedance of the redox couple (I_3^-/I^-).

performance is determined as an average of at least 3 samples. The EIS data in this work are helpful for understanding all composite solar cells, and also can explain well the existing interfaces in DSSCs. It can be clearly seen that R_{ct}, representing interfacial transfer resistance of the counter electrode/electrolyte interface, is 6.45 Ω for DC_1, 5.21 Ω for DC_2, and 7.74 Ω for DC_3. The R_{ct} value of the DC_{Pt} seems too low. This may be due to the application of bias voltage of −0.8 V, which results in the increase of Fermi level of Pt counter electrode. So, it can match the redox potential of the redox shuttle electrolyte better. As a result, the driving force of the electron transferring from the counter electrode to the electrolyte increases, so the electron of the external circuit can transfer to the electrolyte more easily and fast. The less interface resistance will result in faster interfacial electron transfer, which favors the higher η. Among them, the DC_2 displays the fastest electron transfer rate, and thus the highest η. Moreover, the DC_1 has the smallest Z_N value among the Pt-free DSSCs, which indicates a fastest diffusion rate of the redox species in the electrolyte according to eq 4. The EIS results agree with the $J-V$ data. Furthermore, the C_μ values decrease from DC_1 to DC_3, suggesting the reduction of the surface area in order, which coincides with the above BET result.[30]

Tafel-polarization measurement is used to investigate the catalytic activity of the GC/Fe_3C counter electrode with controlled Fe_3C nanoparticle content. Typically, the Tafel curve could be divided into three zones. The curve at low potential ($|U| < 120$ mV) is the polarization zone, the curve at the middle potential (with a sharp slope) is the Tafel zone, and the curve at high potential is the diffusion zone. The information about the exchange current density (J_0) and the limiting diffusion current density (J_{lim}) can be obtained from the latter two curves.[54]

The Tafel curves of the dummy cells (DC_1, DC_2, DC_3, and DC_{pt}) are shown in Figure 11. In the Tafel zone, the tangent

dx.doi.org/10.1021/am4001584 | ACS Appl. Mater. Interfaces 2013, 5, 3663−3670

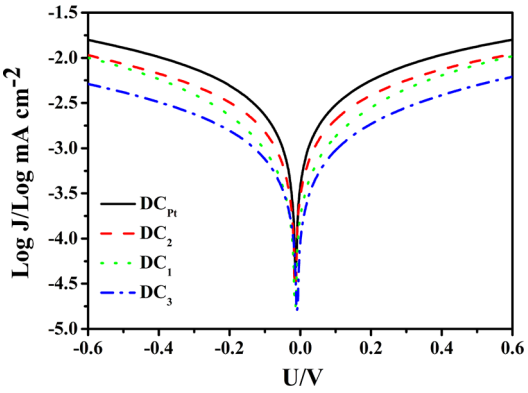

Figure 11. Tafel-polarization curves of the dummy cells (DC_1, DC_2, DC_3, and DC_{pt}) fabricated with two identical E_1, E_2, E_3, and E_{Pt}.

slope of the curve provides information about J_0, which is closely related to R_{ct} value according to eq 5.[55]

$$J_0 = \frac{RT}{nFR_{ct}} \quad (5)$$

Where R is the gas constant, T is the temperature, F is the Faraday constant, and n is the total number of individuals.

The DC_2 exhibits a large J_0 in comparison with that of DC_1 and DC_3, indicating the superior catalytic activity for DC_2 among the three DSSCs with Pt-free counter electrodes. In the diffusion zone, the J_{lim} of the DC_1, DC_2, DC_3, and DC_{Pt} shows the similar magnitude, indicating that similar diffusion properties are available for these catalysts in the electrolyte. J_{lim} varies with the diffusion coefficient (D) according to eq 6

$$J_{lim} = \frac{2neDCN_A}{l} \quad (6)$$

Where D is the diffusion coefficient of I_3^-, l is the spacer thickness, C is the I_3^- concentration, N_A is Avogadro's constant, and e and n have their usual meanings. The Tafel results agree with the EIS and $J-V$ results.

Chart 2 shows the possible catalytic mechanism of GC/Fe_3C counter electrodes with controllable Fe_3C content toward I_3^- reduction. For the GC/Fe_3C cathode with Fe_3C content of 13.5%, the Fe_3C nanoparticles are spread uniformly on the surface of GC, as evidenced by TEM images (Chart 2a). By taking advantage of the fast electron transfer of GC, the photoelectrons are easily shuttled across the GC mat to the catalytic Fe_3C nanoparticle sites where the electrons are used to reduce triiodide. Because of the best dispersion of Fe_3C nanoparticles on the surface of GC, the grain boundary of Fe_3C has the least influence on the electron transfer to the surface of the Fe_3C nanoparticles where I_3^- reduction occurs. So, the GC/Fe_3C cathodes with Fe_3C content of 13.5% possess the best catalytic activity and fastest electron transport, and the DSSCs based on it get the highest η. For the GC/Fe_3C cathode with Fe_3C content of 21.9%, the Fe_3C nanoparticles are aggregated on the surface of GC, which inhibited the delivery of the electrons to the surface of the Fe_3C nanoparticles. So it gets the lower η (Chart 2b). For the GC/Fe_3C cathode with Fe_3C content of 9.4%, less Fe_3C nanoparticles are dispersed on the surface of GC, which resulted in less catalytic activity for the reduction of I_3^- (Chart 2c). On the basis of the aforementioned statements, the GC/Fe_3C cathodes with Fe_3C content of 13.5% displays a higher catalytic activity toward the I_3^- reduction.

Chart 2. Possible Catalytic Mechanism of GC/Fe_3C Cathodes with Controllable Fe_3C Content toward I_3^- Reduction

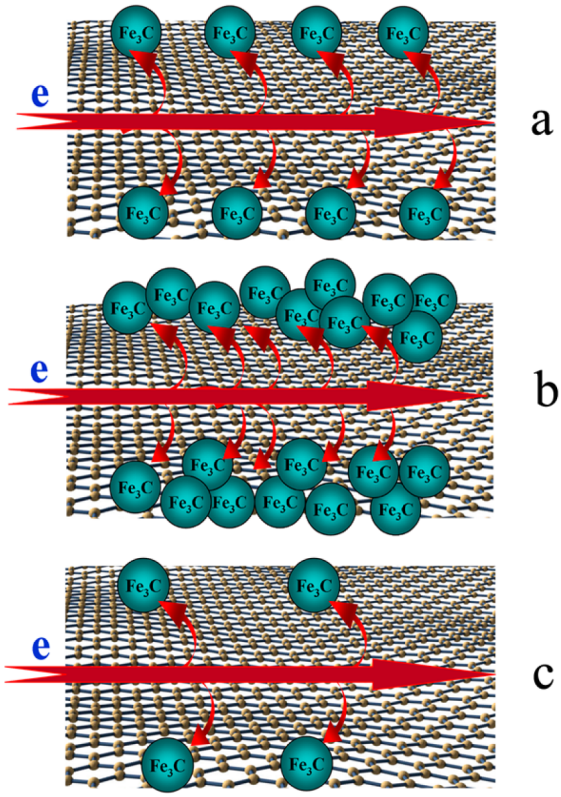

CONCLUSIONS

In this work, the counter electrodes of highly crystalline GC/Fe_3C nanocomposite with controllable Fe_3C content have been prepared. Among these DSSCs made from different Fe_3C content cathodes, the C_2 based on the Fe_3C content of 13.5% counter electrode yields the highest photoelectrical conversion efficiency (η) of 6.04%. On the one hand, that is because the C_2 has successfully held the best merits of the two building blocks, i.e., the fast electron transfer of GC and high catalytic performance of Fe_3C nanoparticles with the moderate Fe_3C content (13.5%). On the other hand, the lower interfacial transfer resistance and the higher catalytic performance are also key factors for C_2 to achieve a higher η. Regarding the comparable η of C_2 to that of the typical Pt-based DSSC (6.40%), the DSSCs fabricated from our nanocomposite cathode materials are expected to exhibit more attractive prospects in the large-scale production because of their much lower cost.

ASSOCIATED CONTENT

Supporting Information

Supplementary figures. This material is available free of charge via the Internet at http://pubs.acs.org.

AUTHOR INFORMATION

Corresponding Author

*Tel.: +86 451 8660 4330. Fax: +86 451 8667 3647. E-mail: kaipan@hlju.edu.cn (K.P.); fuhg@vip.sina.com (H.F.).

Notes

The authors declare no competing financial interest.

■ ACKNOWLEDGMENTS

We gratefully acknowledge the support of this research by the National Natural Science Foundation of China (21001042, 21101060, 51272070, 21031001, 91122018), the Program for New Century Excellent Talents in University (NECT-11-0958, NCET-11-0959), the Excellent Youth of Common Universities of Heilongjiang Province (1252G045), Postdoctoral Research Foundation of Heilongjiang Province (LBH-Q11010, LBH-Q10018).

■ REFERENCES

(1) O'Regan, B.; Grätzel, M. *Nature* **1991**, *353*, 737−740.
(2) Grätzel, M. *Nature* **2001**, *414*, 338−344.
(3) Yella, A.; Lee, H.-W.; Tsao, H. N.; Yi, C.; Chandiran, A. K.; Nazeeruddin, M. K.; Diau, E. W.-G.; Yeh, C. Y.; Zakeeruddin, S. M.; Grätzel, M. *Science* **2011**, *334*, 629−634.
(4) Wang, J.; Lin, Z. *Chem. Mater.* **2010**, *22*, 579−584.
(5) Wu, J. H.; Xiao, Y. M.; Tang, Q. W.; Yue, G. T.; Lin, J. M.; Huang, M. L.; Huang, Y. F.; Fan, L. Q.; Lan, Z.; Yin, S.; Sato, T. *Adv. Mater.* **2012**, *24*, 1884−1888.
(6) Ye, M.; Xin, X.; Lin, C.; Lin, Z. *Nano Lett.* **2011**, *11*, 3214−3220.
(7) Jang, Y. H.; Xin, X.; Byun, M.; Jang, Y. J.; Lin, Z.; Kim, D. H. *Nano Lett.* **2012**, *12*, 479−485.
(8) Papageorgiou, N. *Coord. Chem. Rev.* **2004**, *248*, 1421−1446.
(9) Li, K. X.; Luo, Y. H.; Yu, Z. X.; Deng, M. H.; Li, D. M.; Meng, Q. B. *Electrochem. Commun.* **2009**, *11*, 1346−1349.
(10) Peng, S. J.; Tian, L. L.; Liang, J.; Mhaisalkar, S. G.; Ramakrishna, S. *ACS Appl. Mater. Interfaces* **2012**, *4*, 397−404.
(11) Chen, J. K.; Li, K. X.; Luo, Y. H.; Guo, X. Z.; Li, D. M.; Deng, M. H.; Huang, S. Q.; Meng, Q. B. *carbon* **2009**, *47*, 2704−2708.
(12) Trancik, J. E.; Barton, S. C.; Hone, J. *Nano Lett.* **2008**, *8*, 982−987.
(13) Wen, Z. H.; Wang, Q.; Li, J. H. *Adv. Funct. Mater.* **2008**, *18*, 959−964.
(14) Hong, W. J.; Xu, Y. X.; Lu, G. W.; Li, C.; Shi, G. Q. *Electrochem. Commun.* **2008**, *10*, 1555−1558.
(15) Wang, H.; Hu, Y. H. *Energy Environ. Sci.* **2012**, *5*, 8182−8188.
(16) Chang, H. X.; Zhang, H.; Lv, X. J.; Li, J. H. *Electrochem. Commun.* **2010**, *12*, 483−487.
(17) Zhang, H.; Lv, X. J.; Li, Y. M.; Li, J. H. *ACS Nano* **2010**, *4*, 380−386.
(18) Veerappan, G.; Bojan, K.; Rhee, S. W. *ACS Appl. Mater. Interfaces* **2011**, *3*, 857−862.
(19) Wang, J. J.; Zhu, M. Y.; Outlaw, R. A.; Zhao, X.; Manos, D. M.; Holloway, B. C. *Carbon* **2004**, *42*, 2867−2872.
(20) Wang, Y. D.; Wu, M. X.; Lin, X.; Hagfeldt, A.; Ma, T. L. *Eur. J. Inorg. Chem.* **2012**, *22*, 3557−3561.
(21) Jang, J.; Ham, D.; Ramasamy, E.; Lee, J.; Lee, J. S. *Chem. Commun.* **2010**, *46*, 8600−8602.
(22) Li, G. R.; Song, J.; Pan, G. L.; Gao, X. P. *Energy Environ. Sci.* **2011**, *4*, 1680−1683.
(23) Wu, M. X.; Lin, X.; Wang, Y. D.; Wang, L.; Guo, W.; Qi, D. D.; Peng, X. J.; Hagfeldt, A.; Grätzel, M.; Ma, T. L. *J. Am. Chem. Soc.* **2012**, *134*, 3419−3428.
(24) Wu, M. X.; Lin, X.; Hagfeldt, A.; Ma, T. L. *Chem. Commun.* **2011**, *47*, 4535−4537.
(25) Xia, J.; Yuan, J. C.; Yanagida, S. *ACS Appl. Mater. Interfaces* **2010**, *2*, 2136−2139.
(26) Li, J. H.; Zhang, J. Z. *Coordin. Chem. Rev.* **2009**, *253*, 3015−3041.
(27) Wang, M. K.; Anghel, A. M.; Marsan, B.; Ha, N. C.; Pootrakulchote, N.; Zakeeruddin, S. M.; Grätzel, M. *J. Am. Chem. Soc.* **2009**, *131*, 15976−15977.
(28) Sun, H.; Qin, D.; Huang, S.; Guo, X.; Li, D.; Luo, Y.; Meng, Q. *Energy Environ. Sci.* **2011**, *4*, 2630−2637.
(29) Wu, M. X.; Wang, Y. D.; Lin, X.; Yu, N.; Wang, L.; Wang, L. L.; Hagfeldt, A.; Ma, T. L. *Phys. Chem. Chem. Phys.* **2011**, *13*, 19298−19301.
(30) Jiang, Q. W.; Li, G. R.; Gao, X. P. *Chem. Commun.* **2009**, 6720−6722.
(31) Li, G. R.; Wang, F.; Song, J.; Xiong, F. Y.; Gao, X. P. *Electrochim. Acta* **2012**, *65*, 216−220.
(32) Xiao, Y. M.; Wu, J. H.; Lin, J. Y.; Tai, S. Y.; Yue, G. T. *J. Mater. Chem.* **2013**, *1*, 1289−1295.
(33) Li, G. R.; Wang, F.; Jiang, Q. W.; Gao, X. P.; Shen, P. W. *Angew. Chem., Int. Ed.* **2010**, *49*, 3653−3656.
(34) Wu, M. X.; Lin, X.; Hagfeldt, A.; Ma, T. L. *Angew. Chem., Int. Ed.* **2011**, *50*, 3520−3524.
(35) Wen, Z.; Cui, S.; Pu, H.; Mao, S.; Yu, K.; Chen, J. H. *Adv. Mater.* **2011**, *23*, 5445−5450.
(36) Dou, Y. Y.; Li, G. R.; Song, J.; Gao, X. P. *Phys. Chem. Chem. Phys.* **2012**, *14*, 1339−1342.
(37) Liu, C. J.; Tai, S. Y.; Chou, S. W.; Yu, Y. C.; Chang, K. D.; Wang, S.; Chien, F. S. S.; Lin, J. Y.; Lin, T. W. *J. Mater. Chem.* **2012**, *22*, 21057−21064.
(38) Wang, Y. G.; Davis, B. H. *Appl. Catal., A* **1999**, *180*, 277−285.
(39) Kraupner, A.; Antonietti, M.; Palkovits, R.; Schlicht, K.; Giordano, C. *J. Mater.Chem.* **2010**, *20*, 6019−6022.
(40) Wang, L.; Tian, C. G.; Wang, H.; Ma, Y. G.; Wang, B. L.; Fu, H. G. *J. Phys. Chem. C* **2010**, *114*, 8727−8733.
(41) Hagfeldt, A.; Grätzel, M. *Acc. Chem. Res.* **2000**, *33*, 269−277.
(42) Nazeerudin, M. K.; Kay, A.; Rodicioet, I.; Baker, R. H.; Müller, E.; Liska, P.; Vlachopoulos, N.; Grätzel, M. *J. Am. Chem. Soc.* **1993**, *115*, 6382−6390.
(43) Doeff, M. M.; Wilcox, J. D.; Yu, R.; Aumentado, A.; Marcinek, M.; Kostecki, R. *J. Solid. State. Electrochem.* **2008**, *12*, 995−1001.
(44) Papageorgiou, N.; Maier, W. F.; Gratzel, M. *J. Electrochem. Soc.* **1997**, *144*, 876−884.
(45) Ma, T.; Fang, X.; Akiyama, M.; Inoue, K.; Noma, H.; Abe, E. *J. Electroanal. Chem.* **2004**, *574*, 77−83.
(46) Fang, X.; Ma, T.; Guan, G.; Akiyama, M.; Kida, T.; Abe, E. *J. Electroanal. Chem.* **2004**, *570*, 257−263.
(47) Huang, Z.; Liu, X. Z.; Li, K. X.; Li, D. M.; Luo, Y. H.; Li, H.; Song, W. B.; Chen, L. Q.; Meng, Q. B. *Electrochem. Commun.* **2007**, *9*, 596−598.
(48) Sun, H. C.; Luo, Y. H.; Zhang, Y. D.; Li, D. M.; Yu, Z. X.; Li, K. X.; Meng, Q. B. *J. Phys. Chem. C* **2010**, *114*, 11673−11679.
(49) Joseph, D. R.; David, J. B.; Christian, P.; Ilhan, A. A. *ACS Nano* **2010**, *4*, 6203−6211.
(50) Hsieh, C. K.; Tsai, M. C.; Yen, M. Y.; Su, C. Y.; Chen, K. F.; Ma, C. C. M.; Chen, F. R.; Tsai, C. H. *Phys. Chem. Chem. Phys.* **2012**, *14*, 4058−4061.
(51) Hauch, A.; Georg, A. *Electrochim. Acta* **2001**, *46*, 3457−3466.
(52) Yoon, C. H.; Vittal, R.; Lee, J.; Chae, W. S.; Kim, K. J. *Electrochim. Acta* **2008**, *53*, 2890−2896.
(53) Wu, M. X.; Bai, J.; Wang, Y. D.; Wang, A. J.; Lin, X.; Wang, L.; Shen, Y. H.; Wang, Z. Q.; Hagfeldt, A.; Ma, T. L. *J. Mater. Chem.* **2012**, *22*, 11121−11127.
(54) Wang, L.; Diau, E. W.-G.; Wu, M. X.; Lu, H.-P.; Ma, T. L. *Chem. Commun.* **2012**, *48*, 2600−2602.
(55) Zakeeruddin, S. M.; Grätzel, M. *Adv. Funct. Mater.* **2009**, *19*, 2187−2202.